Int. J. Electron. Commun. (AEÜ) 208 (2026) 156248

Contents lists available at ScienceDirect

International Journal of Electronics and Communications

journal homepage: www.elsevier.com/locate/aeue

Orthonormal splitting of RMS phase error in digitally controlled phase shifters

Francisco Aznar [a,b,*], Uxua Esteban-Eraso [b], Antonio D. Martínez-Pérez [b], Roque Fernández [b], Santiago Celma [b]

[a] Centro Universitario de la Defensa, Ctra. Huesca SN, Academia General Militar, 50090 Zaragoza, Spain
[b] Electronic Engineering and Communications Department, Universidad de Zaragoza, Pedro Cerbuna 12, 50009 Zaragoza, Spain

ARTICLE INFO

Keywords:
Array antenna theory
Beamforming
CMOS RF design
Phased array antenna
Phase shifter
RMS phase error

ABSTRACT

Traditionally, the RMS phase error has been the standard metric for assessing the quality of phase shifters used in phased-array beamforming antennas. However, this metric fails to isolate the different effects on the radiation pattern. This work proposes three novel metrics to provide a more nuanced analysis of digitally controlled phase shifters. These metrics, denoted as Beam Steering Error, Null Quality Error, and Side-Lobe Level Error, target specific performance characteristics of the radiation pattern. They are defined for any bit resolution, enabling the decomposition of the RMS phase error into three distinct components, each providing valuable insights into the performance of linear phased arrays. The limitations of conventional RMS phase error analysis are demonstrated, and the advantages of these new metrics are validated through a case study involving a 5-bit architecture implemented in a 65-nm CMOS process, as well as other phase shifters reported in the literature.

1. Introduction

Beamforming plays a critical role in next-generation mobile (5G/6G) and satellite communications [1]. Such systems demand high performance, including highly accurate beam steering. Active antennas based on phased arrays can be employed to provide beamforming capability. In recent years, front-end designs in nanometer CMOS nodes have been proposed to achieve full system integration [2–6].

The phase shifter is the fundamental building block of the electronic front-end of an antenna array for both transmitter and receiver chains [7–11], as it sets the phase distribution along the elements and, consequently, the directivity of the transmitted and received signals. Design considerations have been proposed to minimize sources of phase error [12].

In particular, digitally controlled phase shifters provide a finite number of phase states, which determines the beam steering resolution [13]. The RMS phase error is a widely used quality indicator of the phase shifter performance. However, this error metric does not distinguish between the different alterations induced in the radiation pattern, such as main lobe deviation, high side-lobe levels, and null degradation [14–17].

In many applications, it is nevertheless essential to analyse deviations in specific aspects of the radiation pattern, such as the aforementioned main beam direction, null depth, or side-lobe levels. Unfortunately, the RMS phase error fails to provide a clear understanding of its impact on these specific aspects. In this paper, an ideal linear antenna array is assumed and the impact of the RMS phase error on the radiation pattern is decomposed into three new metrics that account for those effects separately.

Section 2 introduces the RMS phase error as the quality factor of the phased array performance. In Section 3, the proposed metrics are detailed using a complete orthogonal basis applicable to any number of bits. An illustrative example applying the proposed metrics to a 5-bit CMOS phase shifter is presented in Section 4. Two additional digitally controlled phase shifters are further analysed in Section 5. Finally, the main conclusions are drawn in Section 6.

2. RMS phase error

Fig. 1 illustrates the conceptual architecture of a linear j-element array, arranged in a staircase configuration; that is, it follows a progressive phase distribution (PD) with phase step φ. Beam steering in

* Corresponding author.
E-mail addresses: faznar@unizar.es (F. Aznar), uesteban@unizar.es (U. Esteban-Eraso), adimar@unizar.es (A.D. Martínez-Pérez), rfernandez@unizar.es (R. Fernández), scelma@unizar.es (S. Celma).

https://doi.org/10.1016/j.aeue.2026.156248
Received 10 December 2025; Accepted 5 February 2026
Available online 7 February 2026

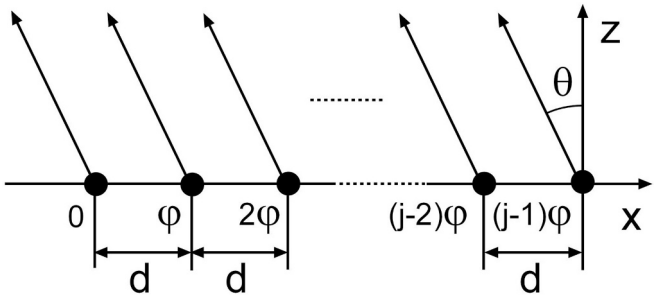

Fig. 1. Linear *j*-element antenna array with a constant inter-element distance *d*. A progressive phase distribution, defined by a step of φ, leads to a constructive interference in the radiation angle θ.

antenna arrays is directly linked to the PD applied to the phase shifters [7]. In this case, the main lobe angle θ resulting from the progressive PD defined by step φ can be calculated using the following equation:

$$\theta = \sin^{-1}\left(\frac{\varphi}{2\pi\frac{d}{\lambda}}\right) \tag{1}$$

where d is the inter-element distance (see Fig. 1) and λ is the wavelength of the transmitted signal. For example, if $d/\lambda = 0.55$, θ equals 3.257° for $\varphi = 11.25°$ (π/16 rad).

2.1. Digitally controlled phase shifters

An m-bit phase shifter defines a phase diagram comprising $n = 2^m$ states and, consequently, a phase resolution of $360°/n$. The ideal phase distribution $\phi^{(n)}$ is therefore a progressive arrangement defined as:

$$\phi^{(n)} = (\phi_0, \phi_1, \ldots, \phi_{n-1}) = \left(0, \frac{360}{n}, \ldots, \frac{(n-1)360}{n}\right) \tag{2}$$

The actual phase of each phase shifter state $\phi_s^{(n)}$ is defined as:

$$\phi_s^{(n)} = (\phi_{s0}, \phi_{s1}, \ldots, \phi_{s,n-1}) \tag{3}$$

Accordingly, the phase error vector is obtained by subtracting the two phase vectors:

$$\Delta\phi^{(n)} = \phi_S^{(n)} - \phi^{(n)} = (\Delta\phi_0, \Delta\phi_1, \ldots, \Delta\phi_{n-1}) \tag{4}$$

Then, to correctly calculate the RMS phase error $\Delta\phi_{\mathrm{RMS}}$, the mean value of the error vector $\overline{\Delta\phi}$ must be accounted for:

$$\overline{\Delta\phi} = \frac{1}{n}\sum_{i=0}^{n-1}\Delta\phi_i \tag{5}$$

$$\Delta\phi_{\mathrm{RMS}} = \sqrt{\frac{1}{n}\sum_{i=0}^{n-1}(\Delta\phi_i - \overline{\Delta\phi})^2} \tag{6}$$

2.2. Effects on phased array performance

The increase in side-lobe level and beam-pointing error due to random array errors have been well-documented in the literature. In [14], it is reported that, to a first-order approximation, amplitude mismatches between phased array channels do not affect the beam-pointing angle; thus, only phase deviations need to be considered for phase steered arrays. Furthermore, if the phase error of each channel is modelled as a normal distribution with standard deviation σ_{phase}, the standard deviation of the beam-pointing deviation σ_{BPD} is given by:

$$\sigma_{\mathrm{BPD}} = \frac{\sqrt{12}}{\pi\cos\theta_m\sqrt{(N-1)N(N+1)}}\sigma_{\mathrm{phase}} \tag{7}$$

where N is the number of elements in the array, θ_m is the ideal beam-pointing angle, and an inter-element distance $d = \lambda / 2$ is assumed. In [7], a simplified equation is reported, and both expressions confirm that σ_{BPD} decreases at a rate proportional to $1/\sqrt{N^3}$.

Regarding the side-lobe level, assuming large arrays with no amplitude error, and phase errors modelled as a normal distribution with standard deviation σ_{phase}, the standard deviation of side-lobe level (σ_{SLL}) [14] is given by:

$$\sigma_{\mathrm{SLL}} = \frac{138.6}{\sqrt{N}}\frac{\pi}{180}\sigma_{\mathrm{phase}} \tag{8}$$

Consequently, it also reduces as the array size increases, but at a rate proportional to $1/\sqrt{N}$.

Both effects are illustrated in Fig. 2a for a linear phased array consisting of 32 omnidirectional elements with a uniform gain distribution. The figure includes a normal distribution representing phase errors, simulated over 500 iterations (grey lines), and compares them with the ideal pattern (green line). The assumed standard deviation of the phase error σ_{phase} equals 3°, which is consistent with the state of the art in CMOS phase shifters. This leads to an obtained σ_{BPD} and σ_{SLL} of 0.017° and 0.27 dB, respectively, matching (7) and (8): $SLL_{\mathrm{ideal}} \pm 1.283$ ($SLL_{\mathrm{ideal}} \pm 0.27$ dB).

However, this procedure is only applicable assuming a normal phase error distribution and a large number of radiating elements. In practical implementations with a reduced number of radiating elements, these statistical formulas are only partially effective. Furthermore, this method fails to provide information about another important aspect: the null depth of the radiation pattern.

To address this limitation, the following section presents a general method for decomposing the phase error vector of a digitally controlled phase shifter into three new metrics to separately and accurately identify each effect on the radiation pattern.

3. Orthonormal basis

As aforementioned, an m-bit phase shifter defines a phase diagram comprising $n = 2^m$ states. From the obtained phases, a phase error vector can be computed and the RMS phase error can be calculated. Alternatively, an orthonormal basis can be defined as an $n \times n$ matrix $M^{(n)}$ with

- A first normalized vector with all identical elements:

$$\vec{v}_{\mathrm{i}} = \frac{1}{\sqrt{n}}(1, 1, \ldots, 1) \tag{9}$$

This vector has no influence on the radiation pattern; specifically, both the ideal phase distribution $\phi^{(n)}$ and a phase distribution including only a phase error proportional to this vector $\phi^{(n)} \pm C\vec{v}_i$ align with the green curve in Fig. 2.

In addition, by defining the following sequence of n odd integers:

$$x = (n-1, n-3, \ldots, -(n-1)) \tag{10}$$

where

$$\sum_{i=0}^{n-1} x_i^2 = \frac{(n+1)n(n-1)}{3} \tag{11}$$

The orthonormal basis can be completed with the following vectors:

- A second normalized vector with elements defining a constant gradient:

$$\vec{v}_g = \sqrt{\frac{3}{(n+1)n(n-1)}}x \tag{12}$$

Indeed, this vector is inherently orthogonal to $\vec{v}_i$ $\left(\vec{v}_g \cdot \vec{v}_i = 0\right)$. The

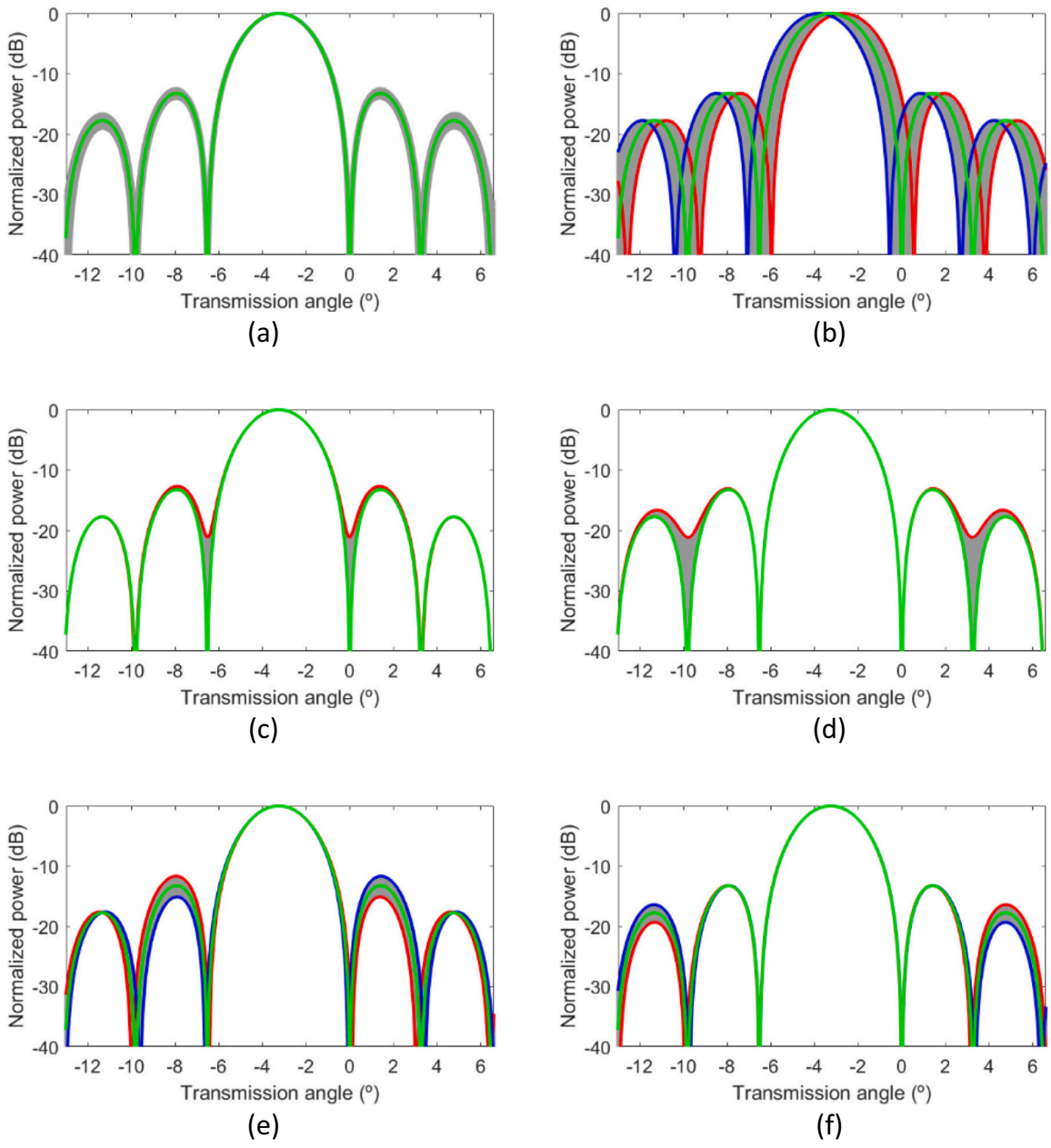

Fig. 2. Radiation patterns for a 32-element linear array with $d/\lambda = 0.55$ and a progressive phase distribution with step $\varphi = 11.25°$ plus phase state errors: based on a normal distribution with $\sigma = 3°$ (a), and only including an error proportional to a vector of the proposed basis: (b) $\vec{v}_g$, (c) $\vec{v}_{s,1}$, (d) $\vec{v}_{s,2}$, (e) $\vec{v}_{a,1}$, (f) $\vec{v}_{a,2}$. The grey area represents the impact on the radiation pattern compared to the ideal case (green line). The red and blue lines (for b, e and f) represent the most extreme cases. (For interpretation of the references to colour in this figure legend, the reader is referred to the web version of this article.)

effect of including this vector $\phi^{(n)} \pm C\vec{v}_g$ in the radiation pattern is illustrated in Fig. 2b. The radiation pattern is horizontally shifted in proportion to the value of C; thus, only the beam pointing direction is affected.

- $\frac{n}{2} - 1$ normalized vectors based on a symmetric distribution *(a, b, c, …, c, b, a)*. In particular, these vectors are defined as:

$$\vec{v}_{s,i} = \sqrt{\frac{2}{n}}\cos(k_{s,i}x) \tag{13}$$

where

$$k_{s,i} = i\frac{\pi}{n} \text{ with } i = 1, 2, \ldots, \frac{n}{2} - 1 \tag{14}$$

These vectors are inherently orthogonal to $\vec{v}_g$, while the values of parameters $k_{s,i}$ lead to be orthogonal to $\vec{v}_i$. As shown in Fig. 2c-d, vectors $\vec{v}_{s,1}$ and $\vec{v}_{s,2}$ cause progressive degradation of the first and second nulls, respectively.

- And $\frac{n}{2} - 1$ normalized vectors defining an antisymmetric distribution *(a, b, c, …, −c, −b, −a)*. In particular,

$$\vec{v}_{a,i} = \sqrt{\frac{2}{n_i}}\sin(k_{a,i}x) \tag{15}$$

where the values of the parameters $k_{a,i}$ are calculated to satisfy the orthogonality condition $\left(\vec{v}_{a,i} \cdot \vec{v}_g = 0\right)$. The analytical solution for the

Table 1
Parameters k_a of the proposed basis for different bit resolutions.

	3 bits: 8 × 8 basis	
$k_{a1} = 0.564697$	$k_{a2} = 0.971091$	$k_{a3} = 1.371288$
	4 bits: 16 × 16 basis	
$k_{a1} = 0.281207$	$k_{a4} = 0.880349$	$k_{a6} = 1.275082$
$k_{a2} = 0.483469$	$k_{a5} = 1.077825$	$k_{a7} = 1.472235$
$k_{a3} = 0.682426$		
	5 bits: 32 × 32 basis	
$k_{a1} = 0.140465$	$k_{a6} = 0.636816$	$k_{a11} = 1.128547$
$k_{a2} = 0.241493$	$k_{a7} = 0.735231$	$k_{a12} = 1.226835$
$k_{a3} = 0.340866$	$k_{a8} = 0.833599$	$k_{a13} = 1.325115$
$k_{a4} = 0.439714$	$k_{a9} = 0.931935$	$k_{a14} = 1.423389$
$k_{a5} = 0.538327$	$k_{a10} = 1.030249$	$k_{a15} = 1.521661$
	6 bits: 64 × 64 basis	
$k_{a1} = 0.070215$	$k_{a12} = 0.613245$	$k_{a22} = 1.104343$
$k_{a2} = 0.120717$	$k_{a13} = 0.662367$	$k_{a23} = 1.153445$
$k_{a3} = 0.170391$	$k_{a14} = 0.711484$	$k_{a24} = 1.202547$
$k_{a4} = 0.219802$	$k_{a15} = 0.760598$	$k_{a25} = 1.251648$
$k_{a5} = 0.269096$	$k_{a16} = 0.809709$	$k_{a26} = 1.300748$
$k_{a6} = 0.318328$	$k_{a17} = 0.858819$	$k_{a27} = 1.349848$
$k_{a7} = 0.367522$	$k_{a18} = 0.907926$	$k_{a28} = 1.398948$
$k_{a8} = 0.416691$	$k_{a19} = 0.957032$	$k_{a29} = 1.448048$
$k_{a9} = 0.465845$	$k_{a20} = 1.006137$	$k_{a30} = 1.497147$
$k_{a10} = 0.514986$	$k_{a21} = 1.055240$	$k_{a31} = 1.546247$
$k_{a11} = 0.564119$		

2-bit architecture is $k_a = \arcsin\sqrt{5/6}$, while the values of $k_{a,i}$ have been computed numerically and are listed in Table 1 for 3-bit to 6-bit architectures. The normalization factor n_i' is then calculated to normalize the vector. The analytical solution for 2-bit is $n' = 100/27$, and $n_i' \approx n$ in all cases.

Thus, the orthonormal basis is completed, as these vectors are inherently orthogonal to $\vec{v}_i$ and the symmetric ones, and satisfy orthogonality to $\vec{v}_g$. As shown in Fig. 2e-f, $\vec{v}_{a,1}$ and $\vec{v}_{a,2}$ only modify the level of the secondary and tertiary lobes, respectively; therefore, the side-lobe level will be primarily defined by $\vec{v}_{a,1}$ at first order.

Consequently, the three proposed metrics are defined from the projections P_i of the phase error vector onto the orthonormal basis:

$$P^{(n)} = M^{(n)}\Delta\phi^{(n)^T}\begin{cases} BSE_{\mathrm{RMS}} = \sqrt{\frac{1}{n}P_1^2} \\ NQE_{\mathrm{RMS}} = \sqrt{\frac{1}{n}\max\left(P_2^2, P_3^2, \ldots, P_{\frac{n}{2}}^2\right)} \\ SLLE_{\mathrm{RMS}} = \sqrt{\frac{1}{n}P_{\frac{n}{2}+1}^2} \end{cases} \tag{16}$$

as beam steering is exclusively associated with projection P_1 ($\vec{v}_g$), null quality is affected by the highest symmetric projection ($\vec{v}_{s,i}$) and side-lobe level is altered by the first antisymmetric projection ($\vec{v}_{a,1}$).

The beam steering error [18] can be expressed in degrees from the product of P_1 and the gradient of the orthonormal vector $\vec{v}_g$, while *NQE* and *SLLE* can be calculated in dB from the corresponding projections using the following expressions:

$$BSE(^\circ) = \frac{2\sqrt{3}}{\frac{2\pi d}{\lambda}\cos\theta_m\sqrt{(n+1)n(n-1)}}P_1 \tag{17}$$

$$NQE(\mathrm{dB}) = -20\log_{10}\frac{\pi}{180\sqrt{2n}}\max\left(|P_2|, \ldots, \left|P_{\frac{n}{2}}\right|\right) \tag{18}$$

$$SLLE(\mathrm{dB}) = \frac{\sqrt{2}}{3\sqrt{n}}P_{\frac{n}{2}+1} \tag{19}$$

Furthermore, the RMS phase error can be calculated from the phase error vector by using (6), or from the projections P_i as follows:

$$\Delta\phi_{\mathrm{RMS}} = \sqrt{\frac{1}{n}\sum_{i=1}^{n-1}P_i^2} \tag{20}$$

Note that projection P_0, related to the vector with all elements identical and to the average of the phase error vector ($P_0 = \sqrt{n}\cdot\overline{\Delta\phi}$), must be omitted.

Assuming that the projections P_i are all random variables following a normal distribution with mean equal 0 and variance σ^2, $\Delta\phi_{\mathrm{RMS}}^2$would follow a random variable distributed by a χ^2, which matches a normal distribution with mean equal σ^2 for increasing n. Under this scenario, the value of $\Delta\phi_{\mathrm{RMS}}$ equals the standard deviation of P_i and, based on the aforementioned equations for beam steering error (17) and side-lobe level error (19), the Eqs. (7)–(8) are fulfilled.

Finally, as some projections included in the RMS phase error (20) are not associated with the new metrics (16), a residual error can be defined as

$$RE_{\mathrm{RMS}}^2 = \Delta\phi_{\mathrm{RMS}}^2 - BSE_{\mathrm{RMS}}^2 - NQE_{\mathrm{RMS}}^2 - SLLE_{\mathrm{RMS}}^2 \tag{21}$$

which quantifies the portion of the phase error that does not appreciably affect the radiation pattern, at least not in its three main aspects. This result is significant because it indicates that the RMS phase error is a conservative metric that tends to overestimate the actual degradation of the radiation pattern.

Next, the proposed metrics are used to analyse how they complement conventional indicators in evaluating the phase distribution quality of a practical digitally controlled phase shifter.

4. Application to a 5-Bit CMOS Phase Shifter

As an example, these metrics are applied to a 5-bit phase shifter implemented in a 65-nm CMOS process [19]. The operating frequency is 19.5 GHz with a working range from 17 to 22 GHz.

4.1. Proposed orthonormal splitting

For a 5-bit architecture, the orthonormal basis consists of 32 vectors: one identical vector, one gradient vector, 15 symmetric vectors, and 15 antisymmetric vectors. From the phased states at 19.5 GHz, $\Delta\phi_{\mathrm{RMS}}$ has been measured and the new metrics have been calculated and are detailed in Table 2. Additionally, the percentage contribution of each metric to the total squared RMS phase error is calculated, for example, $BSE_{\mathrm{RMS}}^2/\Delta\phi_{\mathrm{RMS}}^2$. Notably, the three new metrics are derived from the RMS phase error, revealing that approximately 85% of it is associated with the residual error RE_{RMS}, which does not produce any noticeable effect on the radiation pattern.

The proposed metrics (16) have been calculated for the aforementioned phase shifter and compared to $\Delta\phi_{\mathrm{RMS}}$ over the 17–22 GHz frequency range, as shown in Fig. 3. It can be seen that the frequency dependency of these metrics is distinct from that of the RMS phase error. BSE_{RMS} and $SLLE_{\mathrm{RMS}}$ show a linear decrease with frequency, while NQE_{RMS} presents a minimum over a wide frequency range.

4.2. Verification of metrics

Assuming a linear phased array comprising 32 omnidirectional elements with an ideal gain distribution, the radiation pattern has been

Table 2
Metrics for the phase distribution of the practical phase shifter at 19.5 GHz.

		Proposed splitting			
	$\Delta\phi_{\mathrm{RMS}}$	BSE_{RMS}	NQE_{RMS}	$SLLE_{\mathrm{RMS}}$	RE_{RMS}
(°)	3.13	0.32	0.96	0.69	2.88
(%)	100	1.0	9.4	4.9	84.7

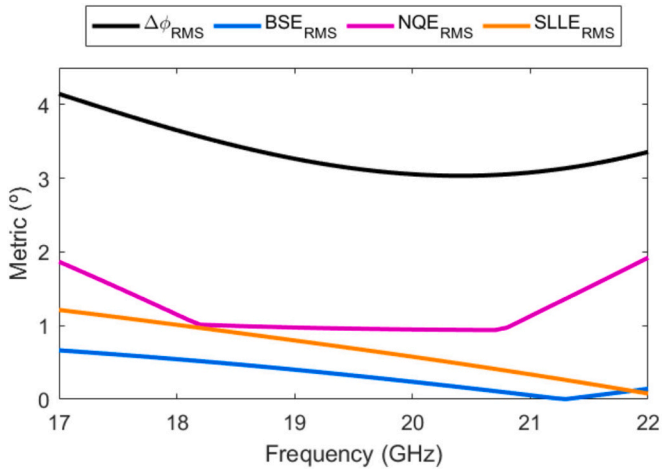

Fig. 3. New metrics and RMS phase error (black) as a function of the frequency for the practical phase shifter: RMS beam steering error (blue), RMS null quality error (magenta) and RMS side-lobe level error (orange). (For interpretation of the references to colour in this figure legend, the reader is referred to the web version of this article.)

evaluated from the phase states of the actual phase shifter. Accordingly, the beam steering angle is defined as the angle corresponding to the maximum power of the radiation pattern, the null quality is quantified by the highest value of the radiation pattern minima, and the side-lobe level is described by the value of the secondary lobe. The results are depicted in Fig. 4 (solid lines). In addition, the proposed metrics (17–19) have been calculated using the orthonormal basis and are also shown in Fig. 4 (dotted lines), effectively predicting the three main aspects of the radiation pattern.

Specifically, the beam steering error (Fig. 4a) shows a perfect match with expression (17). Furthermore, the result crosses the ideal value at 21.3 GHz, achieving a cancellation of BSE_{RMS}, as also shown in Fig. 3.

The null quality of the designed phase shifter, as depicted in Fig. 4b, presents a high value at the center of the evaluated frequency range (from approximately 18 to 20.8 GHz) and shows significant degradation at lower and higher frequencies. Metric (18) is well-suited for the entire frequency range, and accurately predicting both effects as shown in Fig. 3.

The side-lobe level (Fig. 4c) shows a linearly increasing dependence on frequency, tending toward the ideal value at higher frequencies. This behaviour is consistent with the values calculated from metric (19), attaining almost null values at 22 GHz as predicted by $SLLE_{RMS}$ in Fig. 3.

These results demonstrate how the proposed metrics can be used to isolate the main aspects of the radiation pattern and study their distinct behaviour with frequency [20]. It is important to note that, when using only the RMS phase error, the design cannot be optimized to achieve, for instance, zero beam steering error at a given frequency.

5. Analysis of other phase shifters

The same methodology has been applied to two additional digitally controlled phase shifters to further evaluate their phase error performance.

First, the metrics have been calculated for another 5-bit shifter implemented in a 65-nm CMOS process [21]. The operating frequency is 28 GHz with a working range from 24 to 30 GHz. The metrics for the operating frequency are reported in Table 3, while the results are depicted in Fig. 5. In this case, the RMS phase error remains approximately constant as a function of the frequency. Furthermore, *NQE* is also approximately constant and represents the predominant error, while *BSE* and *SLLE* are minimal. The residual error accounts for above 70% of the total error at the operating frequency.

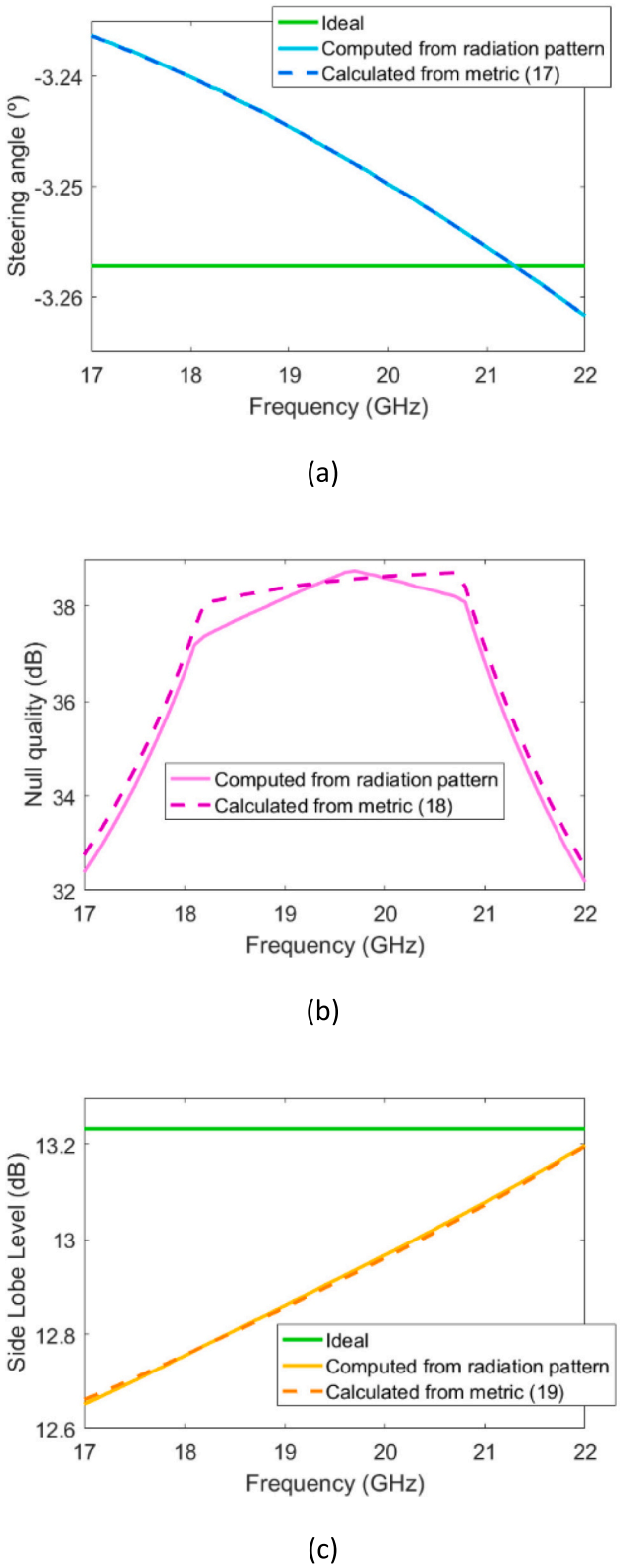

Fig. 4. (a) Beam steering angle (blue), (b) null quality (magenta) and (c) side lobe level (orange) as a function of the frequency for a 5-bit digitally controlled phase shifter. The values computed from the radiation pattern (solid lines) are compared to the calculated values from metric (dotted lines) and the ideal value (green lines). (For interpretation of the references to colour in this figure legend, the reader is referred to the web version of this article.)

Table 3
Metrics for the phase distribution of the phase shifter [21] at 28 GHz.

		Proposed splitting			
	$\Delta\phi_{RMS}$	BSE_{RMS}	NQE_{RMS}	$SLLE_{RMS}$	RE_{RMS}
(°)	2.07	0.08	1.11	0.06	1.75
(%)	100	0.2	28.5	0.1	71.2

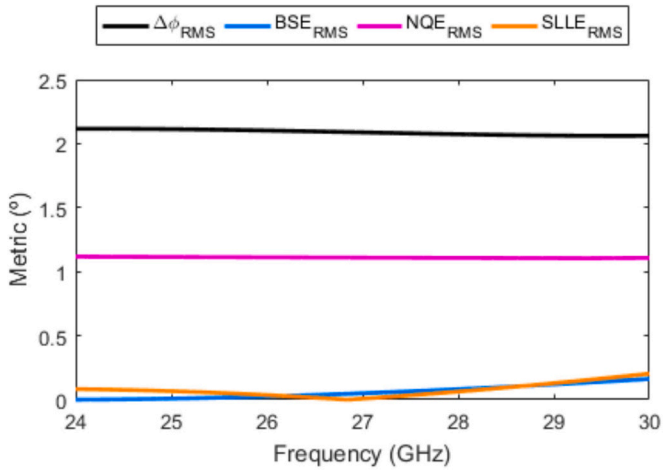

Fig. 5. New metrics and RMS phase error (black) as a function of the frequency for the phase shifter [21]: RMS beam steering error (blue), RMS null quality error (magenta) and RMS side-lobe level error (orange). (For interpretation of the references to colour in this figure legend, the reader is referred to the web version of this article.)

Table 4
Metrics for the phase distribution of the phase shifter [22] at 90 GHz.

		Proposed splitting			
	$\Delta\phi_{RMS}$	BSE_{RMS}	NQE_{RMS}	$SLLE_{RMS}$	RE_{RMS}
(°)	0.85	0.18	0.30	0.23	0.74
(%)	100	4.5	12.2	7.2	76.1

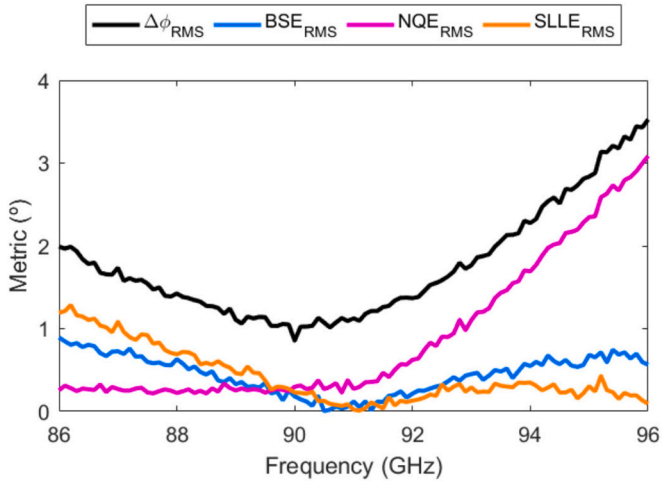

Fig. 6. New metrics and RMS phase error (black) as a function of the frequency for the phase shifter [22]: RMS beam steering error (blue), RMS null quality error (magenta) and RMS side lobe level error (orange). (For interpretation of the references to colour in this figure legend, the reader is referred to the web version of this article.)

Subsequently, a 6-bit phase shifter implemented in a 28-nm CMOS process [22] was analysed. The operating frequency is 90 GHz with a working range from 86 to 96 GHz. The metrics for the operating frequency are provided in Table 4, and the results are depicted in Fig. 6. In this case, the RMS phase error is optimized for the operating frequency, and the three metrics (*BSE*, *SLLE*, and *NQE*) present quite similar contributions. The RMS phase error degrades at higher frequencies due to increased *NQE* and at lower frequencies due to *BSE* and *SLLE*. The residual error is approximately 75% at the operating frequency.

6. Conclusions

Phase shifter performance is critical to the effective implementation of beamforming in antenna arrays. To compare phase shifters, the RMS phase error is conventionally used as a quality metric of the phase distribution. However, as a global metric, it does not provide a comprehensive understanding of its impact on the radiation pattern topology. Depending on the application, it is essential to determine how phase inaccuracies affect specific aspects of the radiation pattern. In this work, three new metrics have been defined, isolating from the phase error the contribution to the three critical aspects: beam steering accuracy, null quality, and side-lobe level.

As a case study, these metrics have been used to characterize three different phase shifters manufactured in CMOS technology. The results reveal that a significant portion of the RMS phase error (approximately 70–85% in the analysed cases) is not associated with any meaningful aspect of the radiation pattern. Consequently, the conventional RMS phase error considerably overestimates degradation and fails to discern critical distortions in the radiation pattern. Additionally, decomposing the phase error into three fundamental components enables the study of their individual frequency dependencies, facilitating design optimization tailored to specific performance requirements.

In conclusion, the traditional RMS phase error is not the most accurate indicator of phase shifter quality; instead, the proposed metrics provide a more precise and insightful characterization. While the definitive acceptance of these metrics will require extensive experimental validation on complete systems, such validation is beyond the scope of the present work.

Future research will extend the proposed framework to two-dimensional phased-array antennas using a tensor-based formulation derived from the proposed basis. This extension is particularly relevant for architectures relying on element-wise phase control. Practical non-idealities, including mutual coupling and amplitude mismatch, will also be incorporated to further enhance the applicability of the proposed framework in realistic operating environments.

CRediT authorship contribution statement

Francisco Aznar: Writing – review & editing, Writing – original draft, Visualization, Validation, Supervision, Software, Project administration, Methodology, Investigation, Funding acquisition, Formal analysis, Conceptualization. **Uxua Esteban-Eraso:** Writing – review & editing, Resources, Investigation, Data curation. **Antonio D. Martínez-Pérez:** Writing – review & editing, Resources, Investigation, Data curation. **Roque Fernández:** Writing – review & editing. **Santiago Celma:** Writing – review & editing, Validation, Supervision, Project administration, Funding acquisition.

Declaration of competing interest

The authors declare that they have no known competing financial interests or personal relationships that could have appeared to influence the work reported in this paper.

Acknowledgements

The authors would like to thank Parsa Tahbazalli [21] and Dongfang Pan [22] for sharing the data necessary for this study. This work was supported in part by the Spanish State Research Agency (PID2020-114110RA-I00 and PID2023-150244OB-I00) and the Centro Universitario de la Defensa Zaragoza (CUD-2025_01).

Data availability

Data will be made available on request.

References

[1] Hueber G, Niknejad AM. Millimeter-wave circuits for 5G and radar, The Cambridge RF and Microwave Engineering Series. Cambridge University Press; 2019.
[2] Gao L, Rebeiz GM. A 22–44-GHz phased-Array receive Beamformer in 45-nm CMOS SOI for 5G applications with 3–3.6-dB NF. IEEE Trans Microwave Theory Tech Nov. 2020;68(11):4765–74. https://doi.org/10.1109/TMTT.2020.3004820.
[3] Wang Y, et al. A 39-GHz 64-element phased-array transceiver with built-in phase and amplitude calibrations for large-array 5G NR in 65-nm CMOS. IEEE J Solid State Circuits May 2020;55(5):1249–69. https://doi.org/10.1109/JSSC.2020.2980509.
[4] Fakharzadeh M, Nezhad-Ahmadi M-R, Biglarbegian B, Ahmadi-Shokouh J, Safavi-Naeini S. CMOS phased Array transceiver technology for 60 GHz wireless applications. IEEE Trans Antennas Propag April 2010;58(4):1093–104. https://doi.org/10.1109/TAP.2010.2041140.
[5] J. Pang et al., "A 28-GHz CMOS phased-array beamformer utilizing neutralized bi-directional technique supporting dual-polarized MIMO for 5G NR," IEEE J Solid State Circuits, vol. 55, no. 9, pp. 2371–2386, Sept. 2020, doi:https://doi.org/10.1109/JSSC.2020.2995039.
[6] Ortiz JA, Salazar-Cerreno JL, Díaz JD, Lebrón RM, Aboserwal NA, Jeon L. Low-cost CMOS active Array solution for highly dense X-band weather radar network. IEEE Trans Antennas Propag July 2020;68(7):5421–30. https://doi.org/10.1109/TAP.2019.2947135.
[7] Mailloux RJ. Phased Array antenna handbook. 2nd ed. Artech House; 2005.
[8] Zhang Z, Leng Y, Qiu X, Yang S, Cui X. A UWB vector synthesis phase shifter based on an improved current array control circuit and an RC-RL polyphase filter. AEU-Int J Electron C Feb. 2025;191:155659. https://doi.org/10.1016/j.aeue.2024.155659.
[9] Zhao D, et al. Millimeter-wave integrated phased arrays. IEEE Trans Circuits Syst I Regul Pap Oct. 2021;68(10):3977–90. https://doi.org/10.1109/TCSI.2021.3093093.
[10] Y. Li et al., "A 32–40 GHz 7-bit bi-directional phase shifter with 0.36 dB/1.6° RMS magnitude/phase errors for phased array systems," IEEE Trans Circuits Syst I Regul Pap, vol. 69, no. 10, pp. 4000–4013, Oct. 2022, doi:https://doi.org/10.1109/TCSI.2022.3188157.
[11] Koh K-J, Rebeiz GM. 0.13-um CMOS phase shifters for X-, Ku-, and K-band phased arrays. IEEE J Solid State Circuits Nov. 2007;42(11):2535–46. https://doi.org/10.1109/JSSC.2007.907225.
[12] Morton MA, Comeau JP, Cressler JD, Mitchell M, Papapolymerou J. Sources of phase error and design considerations for silicon-based monolithic high-pass/low-pass microwave phase shifters. IEEE Trans Microwave Theory Tech Dec. 2006;54(12):4032–40. https://doi.org/10.1109/TMTT.2006.886162.
[13] Tang X, et al. Beam steering resolution for large antenna array. In: IEEE international symposium on antennas and propagation and USNC-URSI radio science meeting (APS/URSI), Singapore, Singapore; 2021. p. 273–4. https://doi.org/10.1109/APS/URSI47566.2021.9703975.
[14] Niknejad AM, Hashemi H. Mm-wave silicon technology 60 GHz and beyond. Springer; 2008.
[15] Coviello G, Cannone F, Avitabile G. A study on the phase errors distributions in phased array systems based on a behavioural model of radiation-pattern characteristics. In: Melecon 2010–2010 15th IEEE Mediterranean Electrotechnical Conference, Valletta, Malta; 2010. p. 74–9. https://doi.org/10.1109/MELCON.2010.5476335.
[16] Iye T, Tsuda K, Tanibayashi A, Fujii Y. Evaluation of RF device error factors on the beam directivity of an uniform linear Array antenna. IEICE Commun Express Aug. 2020;9(11):547–52. https://doi.org/10.1587/comex.2020XBL0104.
[17] Yu Y, Baltus PGM, van Roermund AHM. Integrated 60GHz RF beamforming in CMOS. In: Analog Circuits and Signal Processing Series. Springer; 2011.
[18] Aznar F, Esteban-Eraso U, Martínez-Pérez AD, Celma S. A new metric measuring steering accuracy of digitally controlled phase shifters. In: International conference on synthesis, modeling, analysis and simulation methods and applications to circuit design (SMACD), Volos, Greece; 2024. p. 1–4. https://doi.org/10.1109/SMACD61181.2024.10745457.
[19] Esteban Eraso U, Sánchez-Azqueta C, Aldea C, Celma S. A 19.5 GHz 5-bit digitally programmable phase shifter for active antenna arrays. Electronics June 2023;12(13):2862. https://doi.org/10.3390/electronics12132862.
[20] F. Aznar, U. Esteban-Eraso, A. D. Martínez-Pérez, C. Sánchez-Azqueta and S. Celma, "Analysis of Non-Idealities in CMOS RX Front-End for Linear Phased Arrays," 2025 IEEE International Symposium on Circuits and Systems (ISCAS), London, United Kingdom, May 2025, pp. 1–5, doi:https://doi.org/10.1109/ISCAS56072.2025.11044094.
[21] Tahbazalli P. A 28-GHz eight-element phased-array receiver front-end with compact size in 65-nm CMOS technology for 5G new radio. AEU-Int J Electron C Oct. 2023;170:154838. https://doi.org/10.1016/j.aeue.2023.154838.
[22] Zhang X, Deng B, Sun L, Pan D, Cheng L. A W-band 0.18-dB RMS gain and 0.97° phase error active phase shifter in 28-nm CMOS. IEEE Microwave Wireless Technol Lett July 2024;34(7):923–6. https://doi.org/10.1109/LMWT.2024.3398796.